




Article

3D Inversion and Interpretation of Airborne Multiphysics Data for Targeting Porphyry System, Flammefjeld, Greenland

Michael Jorgensen ^{1,2,*} , Michael S. Zhdanov ^{1,2}, Alex Gribenko ¹, Leif Cox ¹ , Henrik E. Sabra ³
and Alexander Prihodko ⁴ 

¹ TechnoImaging, LLC, Salt Lake City, UT 84107, USA; mzhdanov@technoimaging.com (M.S.Z.); alex@technoimaging.com (A.G.); leif@technoimaging.com (L.C.)

² Department of Geology and Geophysics, University of Utah, Salt Lake City, UT 84112, USA

³ Vanguard Geophysics, Trekanten 12, DK-3460 Birkerød, Denmark; henrik@sabra.dk

⁴ Expert Geophysics Limited, Aurora, ON L4G 1G2, Canada; alexander@expertgeophysics.com

* Correspondence: mjorgensen@technoimaging.com

Abstract: The exploration of porphyry deposits in Greenland has become increasingly important due to their significant economic potential. We utilized total magnetic intensity (TMI) and mobile magnetotelluric (MobileMT) airborne data to delineate potential porphyry mineralization zones. The TMI method was employed to map variations in the Earth's magnetic field caused by subsurface geological features, including mineral deposits. By analyzing anomalies in TMI data, potential porphyry targets were identified based on characteristic magnetic signatures associated with mineralized zones. Complementing TMI data, MT airborne surveys provided valuable insights into the electrical conductivity structure of the subsurface. Porphyry deposits exhibited distinct conductivity signatures due to the presence of disseminated sulfide minerals, aiding in their identification and delineation. Integration of the TMI and MobileMT datasets allowed for a comprehensive assessment of porphyry exploration targets in Flammefjeld. The combined approach facilitates the identification of prospective areas with enhanced geological potential, optimizing resource allocation and exploration efforts. Overall, this study demonstrates the efficacy of integrating TMI and MobileMT airborne data for porphyry exploration in Greenland, offering valuable insights for mineral exploration and resource development in the region.



Citation: Jorgensen, M.; Zhdanov, M.S.; Gribenko, A.; Cox, L.; Sabra, H.E.; Prihodko, A. 3D Inversion and Interpretation of Airborne Multiphysics Data for Targeting Porphyry System, Flammefjeld, Greenland. *Minerals* **2024**, *14*, 1130. <https://doi.org/10.3390/min14111130>

Academic Editor: Stanisław Mazur

Received: 21 August 2024

Revised: 17 October 2024

Accepted: 5 November 2024

Published: 8 November 2024



Copyright: © 2024 by the authors. Licensee MDPI, Basel, Switzerland. This article is an open access article distributed under the terms and conditions of the Creative Commons Attribution (CC BY) license (<https://creativecommons.org/licenses/by/4.0/>).

Keywords: airborne geophysics; 3D inversion; porphyry deposits; TMI; MobileMT; mineral systems exploration; magnetic remanence

1. Introduction

Despite Greenland's considerable potential, mining activities there have been relatively limited. However, there is an abundance of metals and numerous mineral occurrences, including several world-class deposits [1]. Mineral exploration and mining in Greenland often take place in remote areas that are distant from existing infrastructure, leading to costly transportation and infrastructure establishment. Overall, Greenland maintains a favorable social license to operate, and an ambitious new mineral strategy could attract further investment in its mining sector [1]. Airborne geophysical methods are ideal for this type of environment. They are completely non-invasive, less expensive than ground exploration, and can overcome Greenland's logistical challenges.

It is commonplace for helicopter geophysical surveys to combine total magnetic intensity (TMI) and electromagnetic measurements on a common platform for efficient simultaneous data collection (e.g., [2–4]). The audio frequency magnetic (AFMAG) system was the original airborne passive method [5]. This system largely fell out of favor due to difficulties with interpretation and repeatability. However, passive electromagnetic systems that use natural fields as a source have advantages over active sources, such as lower system weight and better depth of exploration. Because of this, along with advances in

instrumentation, modeling, and inversion [6,7], passive methods have seen a resurgence, starting with the Z-axis tipper EM system (ZTEM) [8,9]. The recently developed MobileMT system [10] includes reference electric fields at a base station, which allows for direct measurements of the resistivity structure (e.g., [11,12]). These methods can image to greater depths than active EM systems, which made them an important part of the industry movement towards mineral system exploration [13].

To make the best use of collected TMI and EM data, one should invert them to suit the geology and survey configuration. This pertains to both the dimensionality of the modeling and the governing physics. For some environmental studies that involve geology, which can be approximated as layered earth, 1D dimensional inversion codes may be appropriate. For many targets, if not most, a complex 3D geology will be expected. In this case, 3D dimensional modeling and inversion should be used to model the physical behavior of the fields accurately. Otherwise, artifacts and inaccurate results should be expected around strong lateral conductivity contrasts [14,15]. Additionally, many magnetic inversion algorithms assume that remanent magnetism contributes negligibly to response and recover susceptibility only. However, this is often inaccurate, and several inversion methods have been developed to incorporate remanent magnetism [16–20].

We applied the above methods to target a porphyry system. The survey area was 370 km northeast of Tasiilaq, Greenland, over the Flammefjeld Block. Porphyry systems are often large in scale with a magnetic and electrically resistive pluton core surrounded by zones of alteration that are moderately conductive and often non-magnetic [21]. This type of target lends itself to airborne EM and TMI methods. Expert Geophysics, Ltd. flew a 193 line-km survey with their MobileMT and Magnetis system. We applied the EMVision[®] software developed by TechnoImaging to invert the MobileMT data to an electrical resistivity model and the TMI data to a magnetic vector model, and induced and remanent magnetizations. All modeling and inversion were performed in full 3D. The joint interpretation of these 3D models creates a clear picture of a porphyry system. The interpretation was not possible without including full 3D EM effects and remanent magnetism.

2. Flammefjeld Project Overview

2.1. Geophysical Surveys

The Flammefjeld Block is located in East Greenland, approximately 370 km northeast of Tasiilaq, Greenland (Figure 1). The block lies along the Paleoproterozoic Nagssugtoqidian Mobile Belt (NMB), which underlies Archaean crystalline rocks (Figure 2). The Flammefjeld Block study area was surveyed from 20 September to 22 September 2023 by Expert Geophysics Limited using a helicopter-borne system employing both MobileMT and total magnetic intensity (TMI) data acquisition systems. In total, 193 line-km of data were acquired over a 31 km² area, employing 150–300 m spaced survey lines oriented N95E and 1000–1400 m spaced tie lines. Figure 3 shows the survey flight lines, TMI data observed, and location of the EM reference station. All data and model images have been trimmed to a specific license area.

2.2. Geological Background

NMB exhibits distinct features, with multiple shear zones or linear bands where all structural components, like layering, foliation, folding axes, and linear features, predominantly align in an east-northeasterly direction [23]. This mobile belt primarily comprises Archaean gneisses, altered during the Proterozoic era, with the metamorphic intensity increasing towards the belt's core. Additionally, there are supracrustal rocks affected by subsequent tectonic and metamorphic activities, primarily composed of pelitic and semipelitic sediments, alongside minor occurrences of quartzites, calcareous deposits, thin ironstones, and amphibolites. Furthermore, a few Proterozoic basic dykes and intrusions, occurring either synchronously or after tectonic events, are observed within the mobile

belt. Notably, younger sialic magmas are concentrated within a 100 km radius at the belt's central region.



Figure 1. World Imagery view of Greenland. The location of the Flammefjeld Block and Tasiilaq are labeled and shown by red crosses.

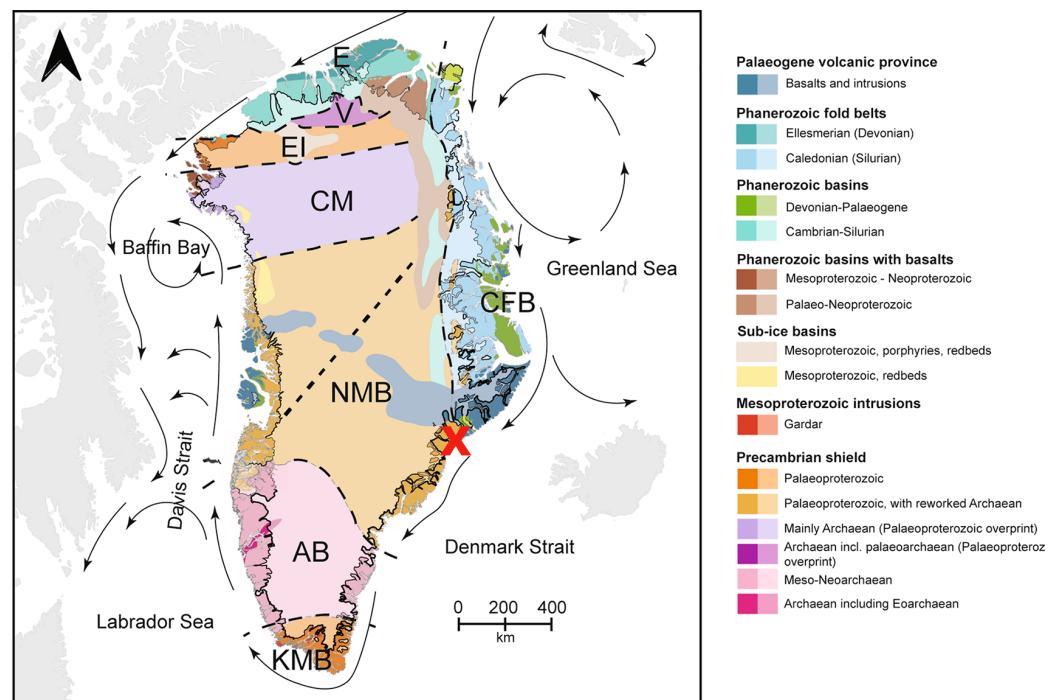


Figure 2. Generalized geology of Greenland, with major geological provinces KMB (Ketildian Mobile Belt), AB (Archean Block), NMB (Nagssugtoqidian Mobile Belt), CM (Committee-Melville), EI (Ellesmere-Inglefield), V (Victoria), E (Ellesmerian), and CFB (Caledonian Fold Belt) indicated. The location of the Flammefield Block is shown by the red cross. Modified from [22].

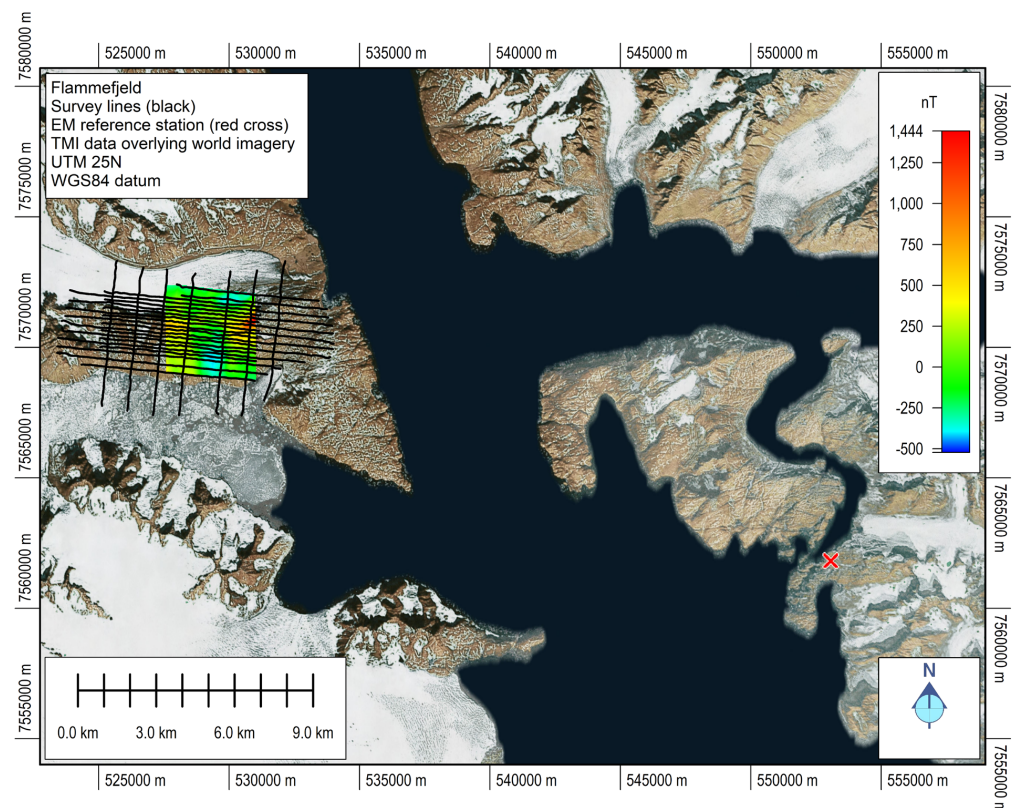


Figure 3. Total magnetic intensity (TMI) data overlain on World Imagery, with the flight path shown in black. The location of the EM reference station is shown by the red cross. The observed data shown have been trimmed to the license area.

During the Paleogene era, the activity of the Iceland mantle plume, coupled with the onset of rifting in the North Atlantic, led to various intrusions occurring in East Greenland, as documented by [24,25]. Among these intrusions is the Kangerlussuaq intrusion, dating back to approximately 50 million years ago, which took the form of an asymmetric lopolith spanning 30 to 35 km in diameter. This intrusion penetrated an unconformity between Archaean gneiss and Paleogene flood basalts, covering roughly 800 square kilometers and comprising the majority of the exposed area of the Kangerlussuaq Alkaline Complex, as noted by [26,27]. Adjacent to its periphery lies the Flammefjeld survey area, housing another younger intrusion, known as the Flammefjeld complex, which intrudes the quartz syenites at the boundary between the Kangerlussuaq intrusion and nearby satellite intrusions (see Figure 4).

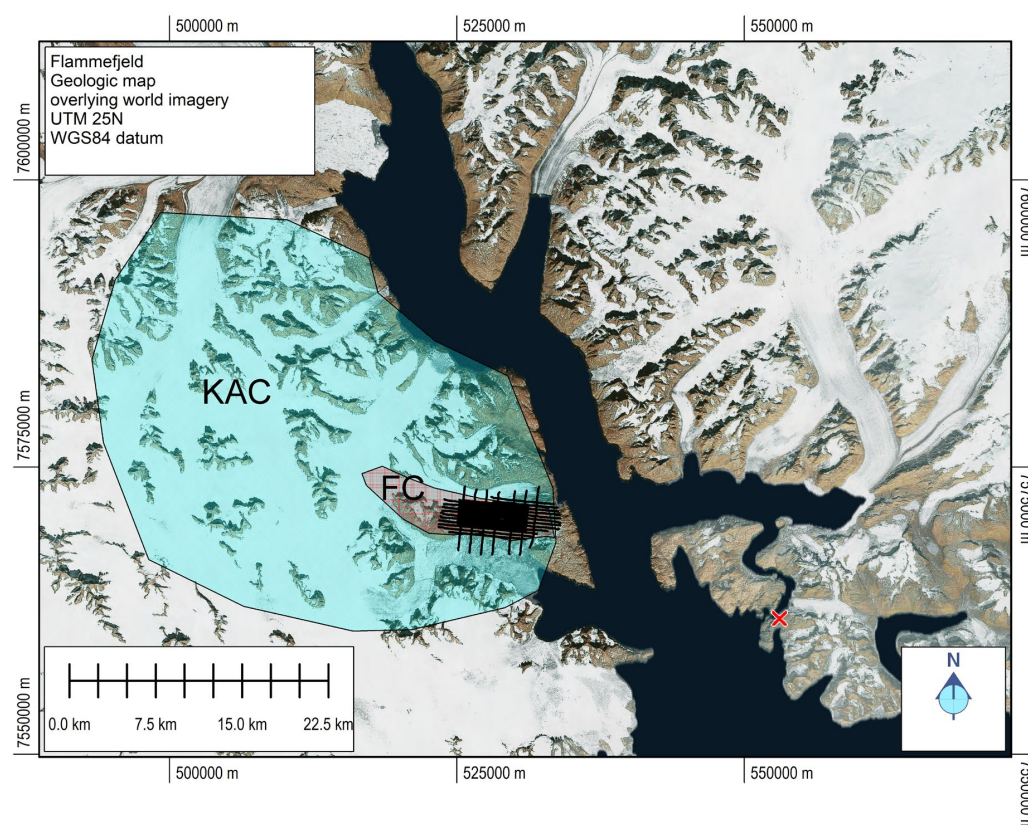


Figure 4. Geological map showing the Kangerlussuaq Alkaline Complex (KAC) in light blue and the Flammefjeld complex (FC) in pink. Flight lines are shown in black and the EM reference station is shown by the red cross.

The Flammefjeld complex is delineated as a composite breccia pipe measuring 500 by 800 m, intruded by quartz-feldspar porphyries, and encircled by a zone of hydrothermal alteration exhibiting vibrant red and yellow oxidation hues, along with distal hydrothermal veins (see Figure 5). These quartz-feldspar porphyries manifest as breccia fragments, constituting a significant intrusive mass and appearing as later dykes. Geological and geochemical investigations indicate the presence of substantial stockwork molybdenum mineralization in the area, as evidenced by the distribution of molybdenum and tungsten, patterns of wall-rock alteration (including quartz-sericite, pyritic, and argillic alterations), and the occurrence of molybdenite mineralization in breccia fragments resembling a stockwork pattern. Proposed geological models envision a concealed Climax-type porphyry molybdenum deposit [28] (refer to Figure 6) positioned approximately 400 to 600 m beneath the survey site. According to these models, the ore body assumes an inverted-saucer configuration, spanning 800 m in diameter and with a thickness of 200 m, featuring molybdenite mineral grades of up to 0.5%.

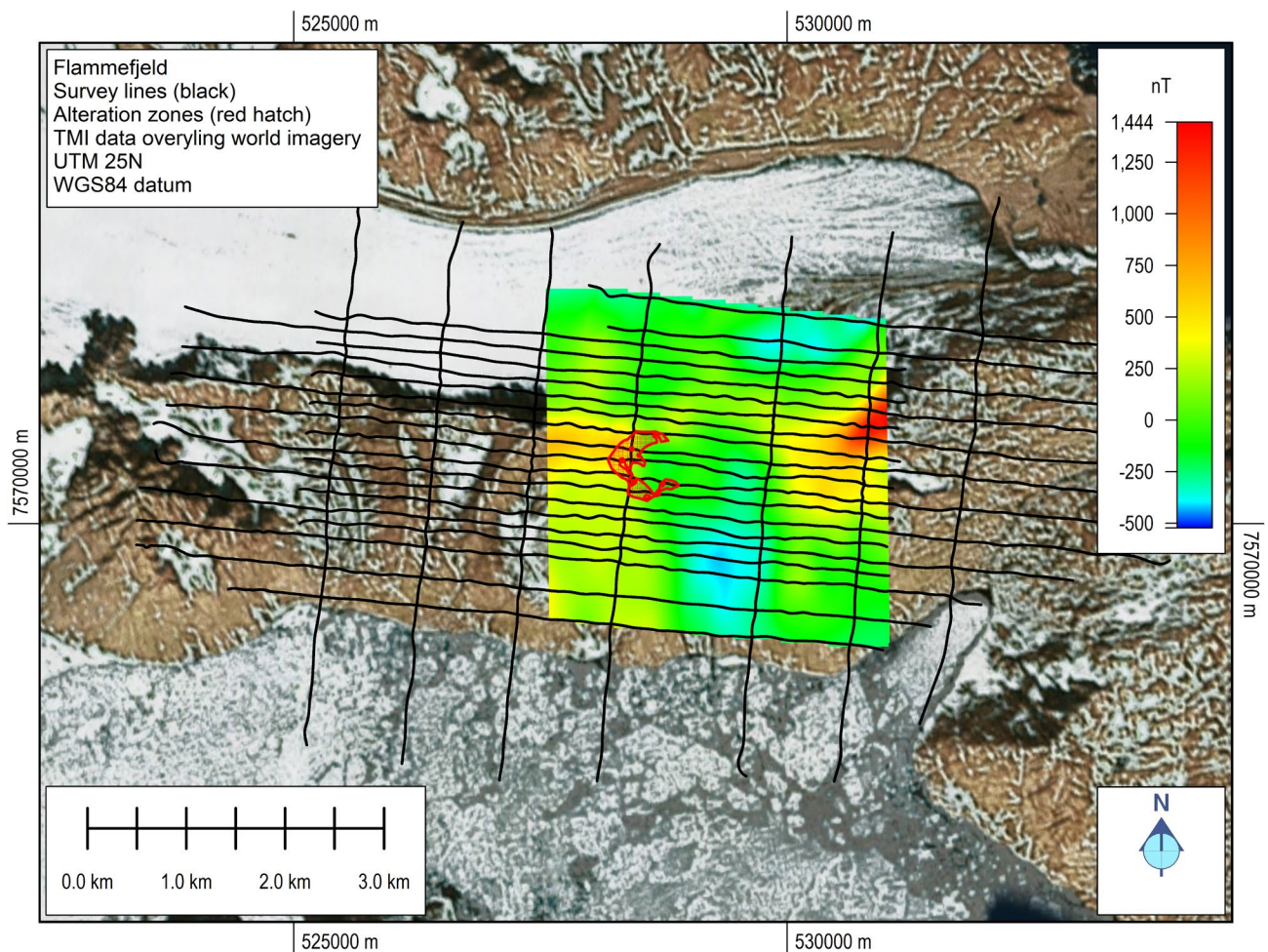


Figure 5. Alteration geology of the survey area, shown in red, overlying the observed TMI data and World Imagery. The survey flight lines are shown in black. The observed data shown have been trimmed to the license area.

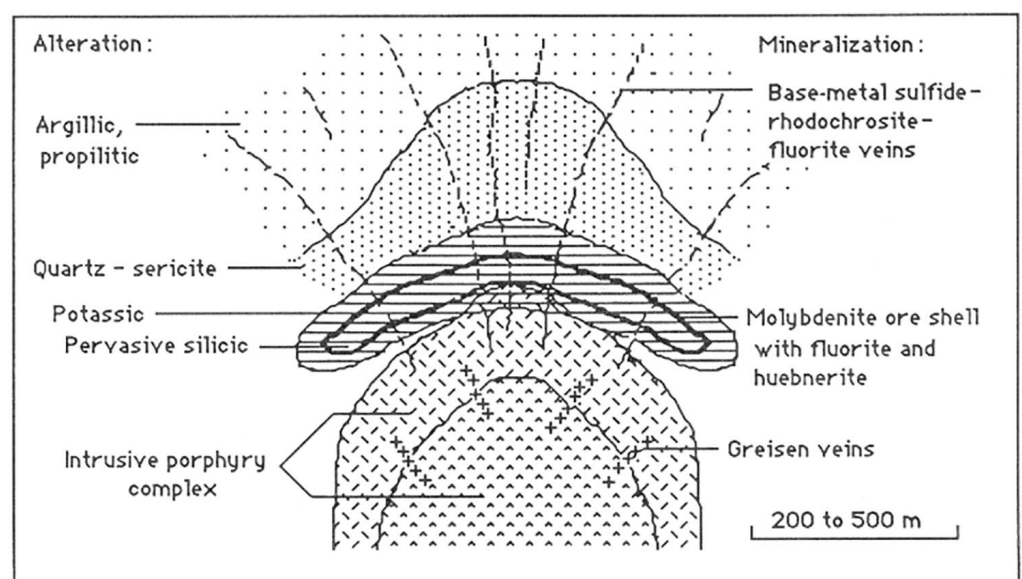


Figure 6. Cartoon cross section of Climax Mo deposit showing the relationship of ore and alteration zoning to porphyry intrusions (after [28]).

3. 3D Inversion of Airborne Magnetic and MT Data

3.1. Inversion of the Magnetic Data into Susceptibility, Induced, and Remanent Magnetizations

The airborne geophysical data used in the study comprised the total magnetic intensity (TMI) data. The data were fully corrected and leveled, with IGRF removal and filtering with a second-degree polynomial to eliminate unwanted regional components of the field.

In mineral exploration, magnetic data have traditionally been inverted to produce magnetic susceptibility models, representing magnetization induced by the current magnetic field. This does not take into account the remanent magnetization of the rocks produced by the ancient magnetic field. More information about rock formations and geological processes can be obtained by inverting magnetic data for magnetization vectors, as opposed to magnetic susceptibility only. In this section, we present a summary of the principles of robust inversion for a magnetization vector using Gramian constraints [17,29].

It is well known that the regularized solution of the geophysical inverse problem can be formulated as the minimization of the Tikhonov parametric functional [30]:

$$P^\alpha(\mathbf{m}) = \varphi(\mathbf{m}) + \alpha S_{MS}(\mathbf{m}) \rightarrow \min, \quad (1)$$

where $\mathbf{m} = \{M_x, M_y, M_z\}$ is the magnetization vector and $\varphi(\mathbf{m})$ is a misfit functional defined as the squared L_2 norm of the difference between the predicted, $A(\mathbf{m})$, and observed, d , data:

$$\varphi(\mathbf{m}) = \|A(\mathbf{m}) - d\|_{L_2}^2. \quad (2)$$

In the last formula, A is the forward modeling operator for the magnetic problem.

The notation S_{MS} in Equation (1) indicates minimum support constraints, which have the effect of focusing the smooth anomalies into compact bodies. This stabilizer is determined as follows [30]:

$$S_{MS}(\mathbf{m}) = \int_V \frac{(m - m_{apr})^2}{(m - m_{apr})^2 + e^2} dv, \quad (3)$$

where e is a focusing parameter, which can be selected using an L-curve method.

Refs. [17,20] demonstrated that in the case of magnetization vector inversion, one should enforce the correlation between the different scalar components of the magnetization vector. This can be achieved by adding the Gramian constraints in the parametric functional (1) as follows:

$$P^\alpha(\mathbf{m}) = \varphi(\mathbf{m}) + \alpha c_1 S_{MS}(\mathbf{m}) + \alpha c_2 \sum_{\beta=x,y,z} S_G(\mathbf{m}_\beta, \chi_{eff}), \quad (4)$$

where \mathbf{m} is the $3N_m$ length vector of magnetization vector components; \mathbf{m}_β is the N_m length vector of the β component of the magnetization vector, $\beta = x, y, z$; and χ_{eff} is the N_m -length vector of the effective magnetic susceptibility, defined as the magnitude of the magnetization vector:

$$\chi_{eff} = \sqrt{M_x^2 + M_y^2 + M_z^2}. \quad (5)$$

Functional S_G is the Gramian constraint:

$$S_G(\mathbf{m}_\beta, \chi_{eff}) = \left| \begin{pmatrix} \mathbf{m}_\beta, \mathbf{m}_\beta & \mathbf{m}_\beta, \chi_{eff} \\ \chi_{eff}, \mathbf{m}_\beta & \chi_{eff}, \chi_{eff} \end{pmatrix} \right|, \quad (6)$$

where $(*,*)_{L_2}$ denotes the L_2 inner product operation.

By employing the Gramian constraint, we establish a direct relationship between the scalar elements of the magnetization vector and χ_{eff} , which is calculated from the prior iteration of the inversion process and is adjusted with each subsequent iteration. The benefit of employing the Gramian constraint as outlined in Equation (6) lies in its

independence of any prior knowledge about the magnetization vector, such as its direction or the interrelation between its different components. This is because the magnitude, χ_{eff} , is derived from the previous iteration. During the initial iteration, the scalar elements are determined separately.

The minimization problem (4) is solved using the re-weighted regularized conjugate gradient (RRCG) method. Details of the RRCG method and conjugate gradient derivations for the parametric functional (4) can be found in [30].

For the decomposition process, we adopt the susceptibility model obtained independently through inversion for susceptibility. We then proceed to multiply this susceptibility with the inducing field unit vector:

$$\mathbf{M}_{ind} = \chi \mathbf{l}(\mathbf{r}),$$

where χ is susceptibility and $\mathbf{l}(\mathbf{r}) = (l_x, l_y, l_z)$ is the unit vector along the direction of the inducing field. Given the inclination (I), declination (D), and azimuth (A) from the International Geomagnetic Reference Field (IGRF), the direction of the inducing magnetic field can be computed as follows (assuming that the x axis is directed eastward, the y axis has a positive direction northward, and the z axis is downward):

$$\begin{aligned} l_x &= \cos(I) \sin(D - A), \\ l_y &= \cos(I) \cos(D - A), \\ l_z &= \sin(I). \end{aligned} \quad (7)$$

Then, remanence is determined by subtracting the induced magnetization from the total magnetization:

$$\mathbf{M}_{rem} = \mathbf{M} - \mathbf{M}_{ind}.$$

3.2. Magnetic Inversion Parameters

A subset of the data was selected for 3D inversion parameter testing. This subset was used to select appropriate voxel sizes for the final inversion based on data sampling and line spacing. The optimal voxel size for this project was determined to be 20 m laterally with a logarithmically spaced vertical discretization. This discretization allowed for higher resolution of near-surface features, minimal line-stripping effects in the inverted models, and a reasonable inversion runtime. The TMI data were then decimated to place one data point over every voxel, which improved the convergence of the inversion.

The starting model for the susceptibility inversion was a homogeneous half-space of 0.0001 SI, and the starting model for the MVI was a homogeneous half-space of vectors with magnitude 0.0001 pointing in the inducing field direction. Focusing regularization was applied to the inversions after the gross geomorphology of the models had taken shape; iteration 10 in the case of susceptibility and iteration 5 in the case of the MVI.

Inversions ran until they reached a data misfit of 5%; however, there was significant noise fitting in the form of spurious near-surface inhomogeneity at the 5% error level. Previous iterations corresponding to roughly 7% data fit were chosen for the final susceptibility and MVI models in which the noise-fitting effects were absent. The observed and predicted TMI data are shown in Figure 7.

3.3. MobileMT Data Modeling

In the framework of the MobileMT method, the magnetic field components were measured in the airborne platform, while the electric field components were recorded in the base station on the ground. The Mobile MT field components can be related through MT transfer functions [10,12]:

$$H_x = Y_{xx}E_x + Y_{xy}E_y, \quad (8)$$

$$H_y = Y_{yx}E_x + Y_{yy}E_y, \quad (9)$$

where (E_x, E_y) represent the horizontal components of the electric field in the base station, and (H_x, H_y) are the horizontal components of the magnetic field recorded in the air.

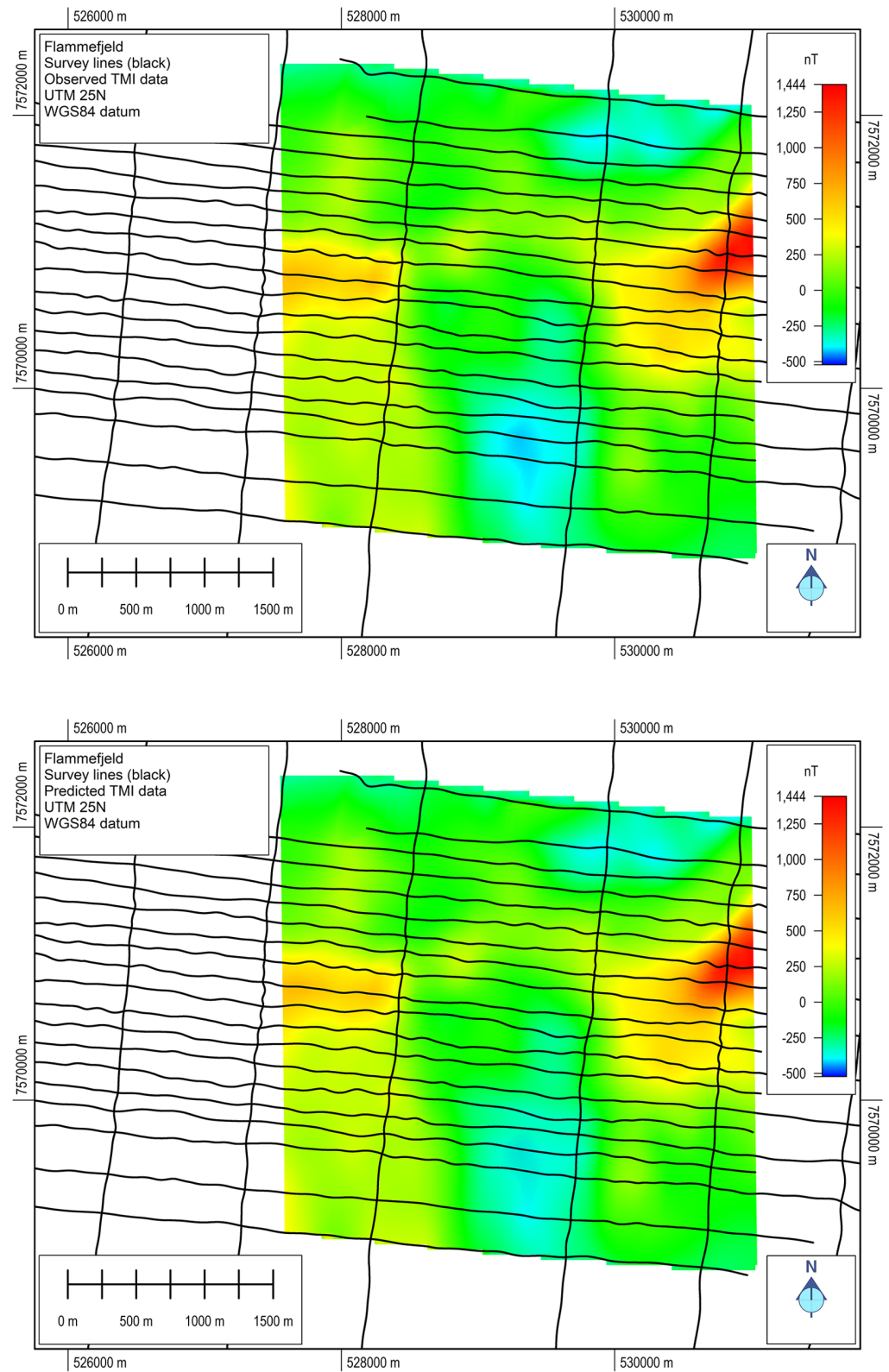


Figure 7. The (top panel) is the observed TMI data after processing. The (bottom panel) is the predicted TMI data. Survey lines are shown in black.

It was demonstrated in the pioneering work of [31] that the transfer functions (Y_{xx} , Y_{xy} , Y_{yx} , Y_{yy}) depend only on the conductivity distribution in the earth and the frequency of the EM field (see also [32]). They form a 2×2 tensor:

$$\mathbf{Y} = \begin{bmatrix} Y_{xx} & Y_{xy} \\ Y_{yx} & Y_{yy} \end{bmatrix}. \quad (10)$$

In the case of the coinciding positions of the magnetic and electric field receivers, this tensor is equal to the classical MT admittance tensor. It is well known that the apparent conductivity and phase can be calculated based on the determinant of admittance tensor using a standard formula [10,12]:

$$\sigma = \mu\omega \left| \left(\det \mathbf{Y} \right)^2 \right|, \quad \varphi = \arg \left(\det \mathbf{Y} \right)^2, \quad (11)$$

where:

$$\det \mathbf{Y} = \sqrt{Y_{xx}Y_{yy} - Y_{xy}Y_{yx}}. \quad (12)$$

The same property holds for the admittance tensor (10) in a general case of different positions of the magnetic and electric field receivers.

Thus, in the framework of the MobileMT method, the apparent conductivity can be obtained from the magnetic field components measured in the air at the location of the bird and horizontal electric field components measured at a reference station located on the ground. Because the magnetic field varies smoothly through conductivity contrasts while the electric field shows discontinuities, the apparent resistivity of the MobileMT system varies more slowly and shows subdued responses relative to what would be expected from a ground-based MT system.

We used the contraction integral equation (CIE) method to calculate EM field components for an arbitrary 3D distribution of the electrical conductivity of the subsurface. The components of the admittance tensor (10) were then found by known analytical formulas [32].

An example of the processed apparent conductivity at 562 Hz is shown in Figure 8.

3.4. MobileMT Data Inversion

The inversion was based on reconstructing the true 3D distribution of the conductivity in the subsurface, which generated the data with the observed apparent resistivities or conductivities. We can see from Equations (8)–(12) that EM field components E and H need to be measured to calculate the admittance tensor values. We used the contraction integral equation (CIE) [32] method to calculate EM field components for an arbitrary 3D distribution of the electrical conductivity of the subsurface. The forward problem can be represented using operator notations as follows:

$$\mathbf{d} = \mathbf{A}(\sigma) \quad (13)$$

where \mathbf{A} is the forward operator based on MT transforms and the CIE method. In the case of inverse modeling, one is trying to find an unknown physical parameter distribution based on the data measured in the field. In our case, conductivity is the physical parameter of interest, and observed data are the Mobile MT apparent conductivities.

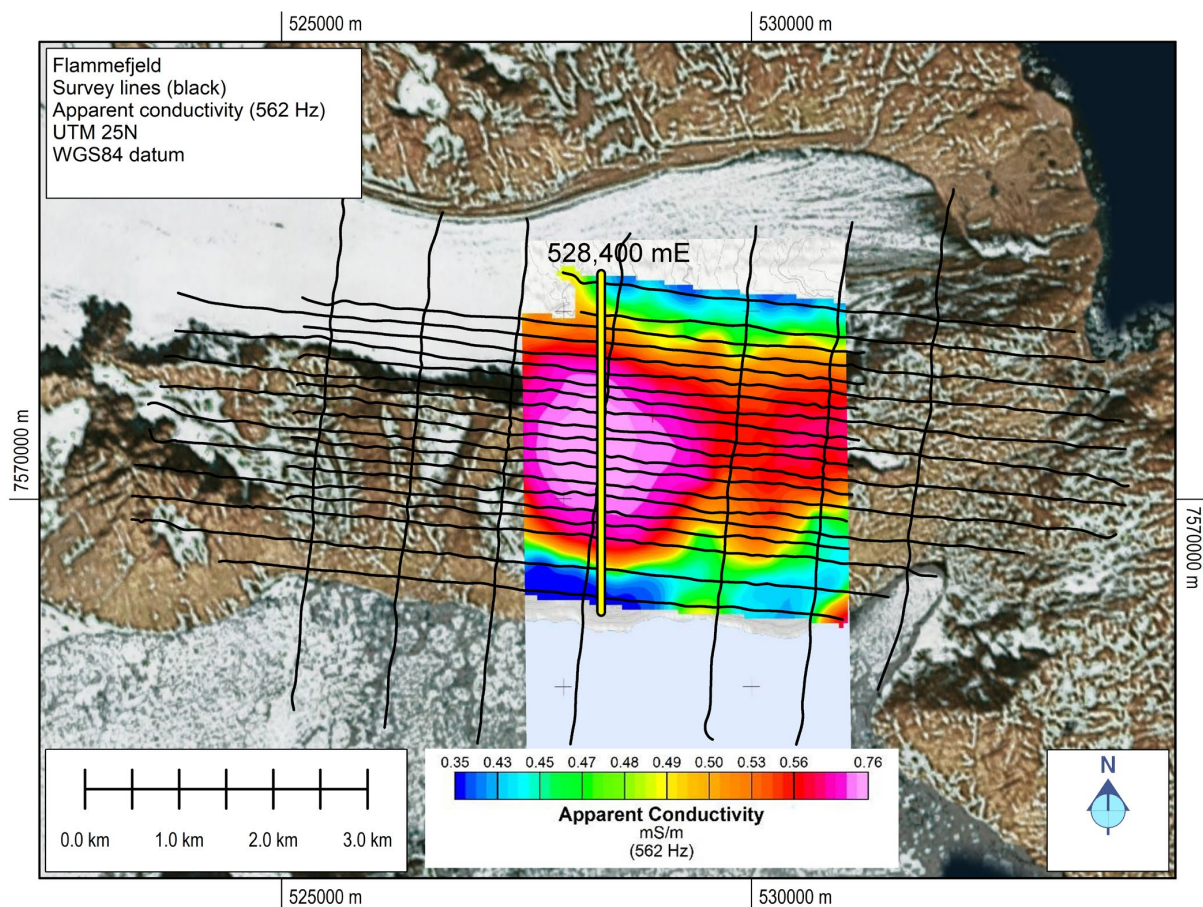


Figure 8. Measured apparent conductivity data at 562 Hz. The flight lines are shown in black. The N/S profile at 528,400 mE is shown in yellow. This profile line corresponds to the vertical model sections shown below. The observed data shown have been trimmed to the license area.

We applied the standard Tikhonov regularization approach [30] to find a conductivity distribution that fit the observed data to an acceptable misfit level. Within the Tikhonov regularization framework, we minimized parametric functional $P(\sigma)$ containing two terms—data misfit $\|r\|^2$ and stabilizer $\|S\|^2$ (model misfit)—with regularization parameter α used to balance the input of the two terms:

$$P(\sigma) = \|r\|^2 + \alpha \|S\|^2 \quad (14)$$

$$r = W_d(A(\sigma) - d_{obs}) \quad (15)$$

$$S = W_m L(\sigma - \sigma_{ref}) \quad (16)$$

$$W_m = \text{diag}(F^T F)^{0.25} \quad (17)$$

In the above equations, W_d represents data weights based on the inverse of variances or the data noise floor, σ_{ref} is the reference conductivity model, L is the first-order finite difference matrix, and F is the Fréchet derivative (sensitivity) matrix.

We used the Newton method in data space to minimize the parametric functional. The Newton method ensures fast convergence and optimal computer memory management. The Fréchet derivatives (sensitivities) of EM fields concerning conductivities are computed via quasi-Born approximation:

$$F_{\sigma}^{E,H} = G_{E,H} E_D \quad (18)$$

Quasi-Born approximation does not require any additional forward modeling to obtain the sensitivity matrix. All necessary values are calculated during CIE forward modeling.

The chain rule is applied to obtain the Fréchet derivatives for impedances. For more details on the MobileMT inversion, please see [6,32–34].

The numerical modeling and inversion methods introduced above were implemented in the EMVision[®] software package, which was used for the interpretation of the MobileMT data.

3.5. MobileMT Inversion Parameters

The MobileMT ground base station where electrical field measurements were conducted was located at the red cross in Figure 3. The system was a four-channel setup (two channels for signal and two channels for reference signal), which measured variations in the electric field in two directions with four pairs of electrodes. The electrical line length was 100 m for each line, with a direction of YX 5 degrees and YZ 97 degrees. The following frequencies were used in the survey (in Hz): 27, 35, 44, 56, 71, 89, 112, 140, 177, 223, 281, 354, 446, 562, 708, 892, 5663, 8990, 11,327, 14,271, 17,980, and 22,654.

A logarithm of apparent resistivity was used as observed data for the inversion. In the inversion, a relative error level of apparent resistivity was assumed to be below 2%. The following frequencies were used in the inversion (in Hz): 35, 44, 71, 89, 112, 177, 223, 281, 446, 562, and 8990.

The lateral cell size was 133×133 m, with 24 logarithmically spaced vertical layers ranging from 14 to 398 m. The initial model for the 3D inversion was obtained by 1D inversions of the data for every receiver. The ocean was not included in the inversion as an a priori model, because the low-frequency data only (up to 100 Hz) may have been affected by the conductive body of the ocean. The skin depth of the lowest frequency was approximately 1.5 km. The distance between the ocean and the main anomaly is well above that distance.

The final overall RMS was 2.45. For most of the stations, RMS is below 1.5. Some of the stations in the east and south show higher values, up to 4. The area of interest is in the middle of the survey area, where the RMS misfits are close to 1. A comparison of the observed and predicted data for selected frequencies is shown in Figure 9.

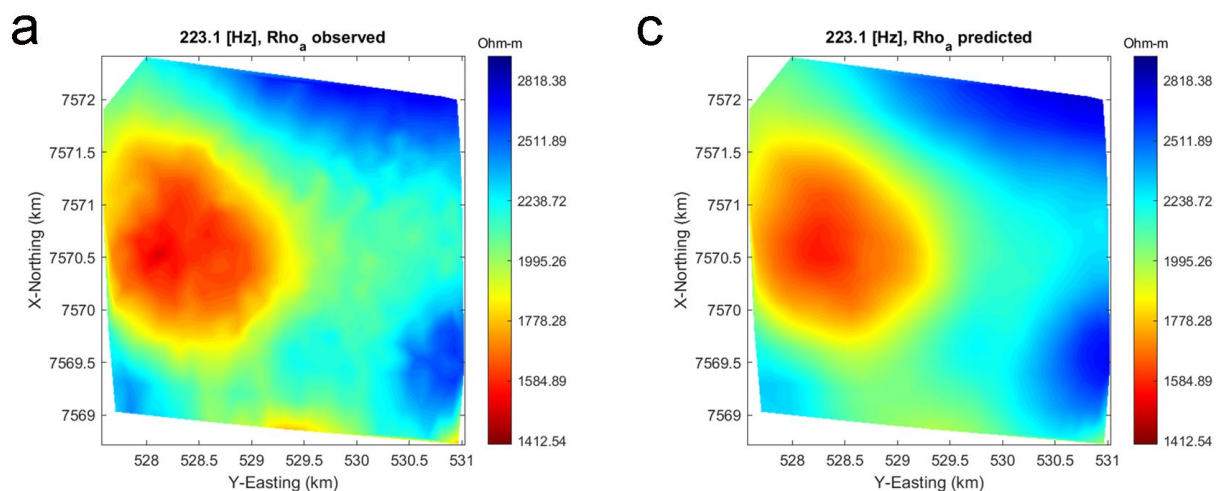


Figure 9. Cont.

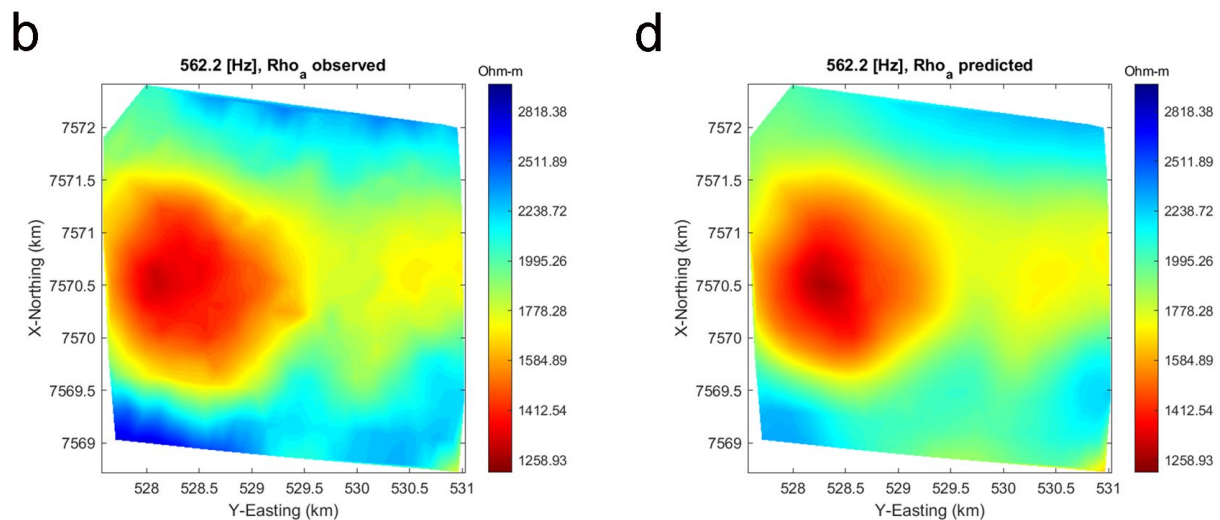


Figure 9. Panels (a,b) show observed apparent resistivity at frequencies 223 and 562 Hz, respectively. Panels (c,d) show the predicted apparent resistivity at the same frequencies.

4. Results of 3D Inversion of the Magnetic and Mobile MT Data

Figures 10–12 show vertical sections of the susceptibility and induced magnetization (the component parallel to Earth's inducing field) and the remanent magnetization inverse models. The induced magnetization can be thought of as an analogue of the susceptibility; however, the distortions due to remanence have been removed. On the other hand, the remanent component contains only the effect of remanence. Figure 10 shows the susceptibility, Figure 11 shows the amplitude of induced magnetization, and Figure 12 shows the amplitude of remanent magnetization. The slice is shown through the center of the identified porphyry system at 528,400 mE, which is shown in yellow in Figure 8.

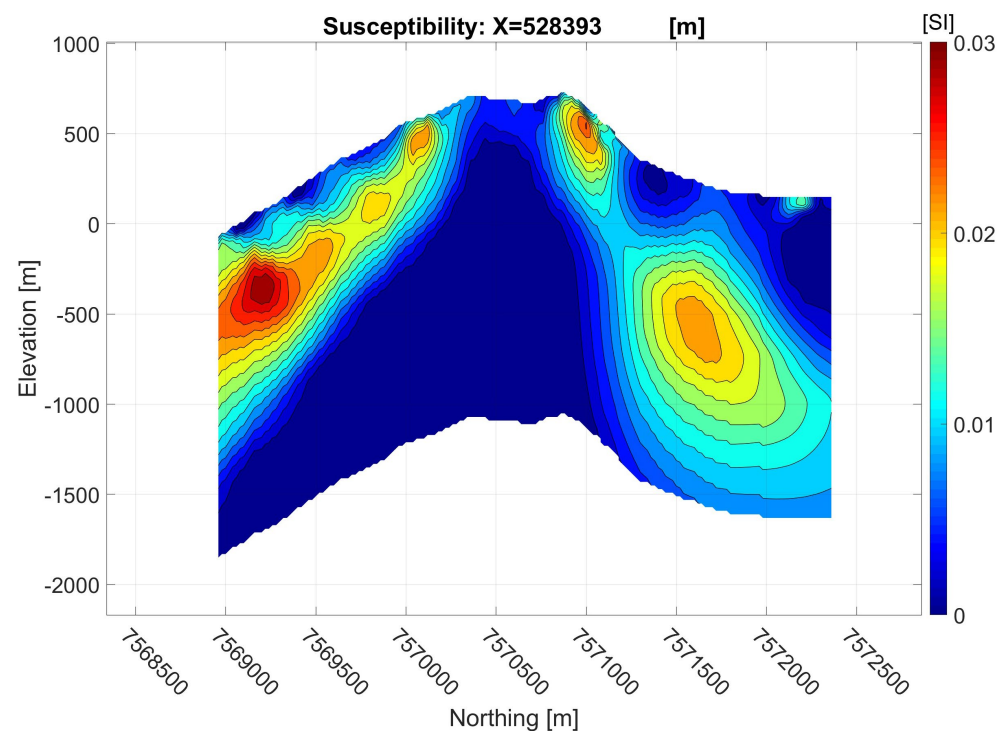


Figure 10. The vertical section was extracted from the 3D voxel model of inverted susceptibility. The location of the profile is shown in yellow in Figure 8.

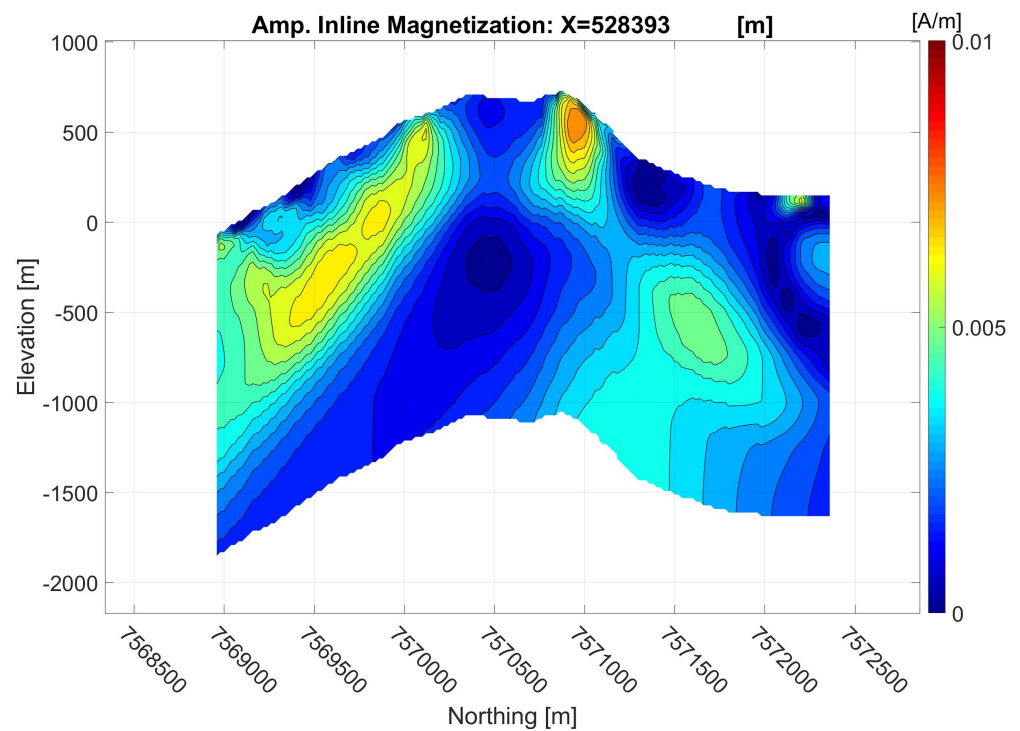


Figure 11. The vertical section was extracted from the 3D voxel model of the inverted amplitude of induced magnetization. The location of the profile is shown in yellow in Figure 8.

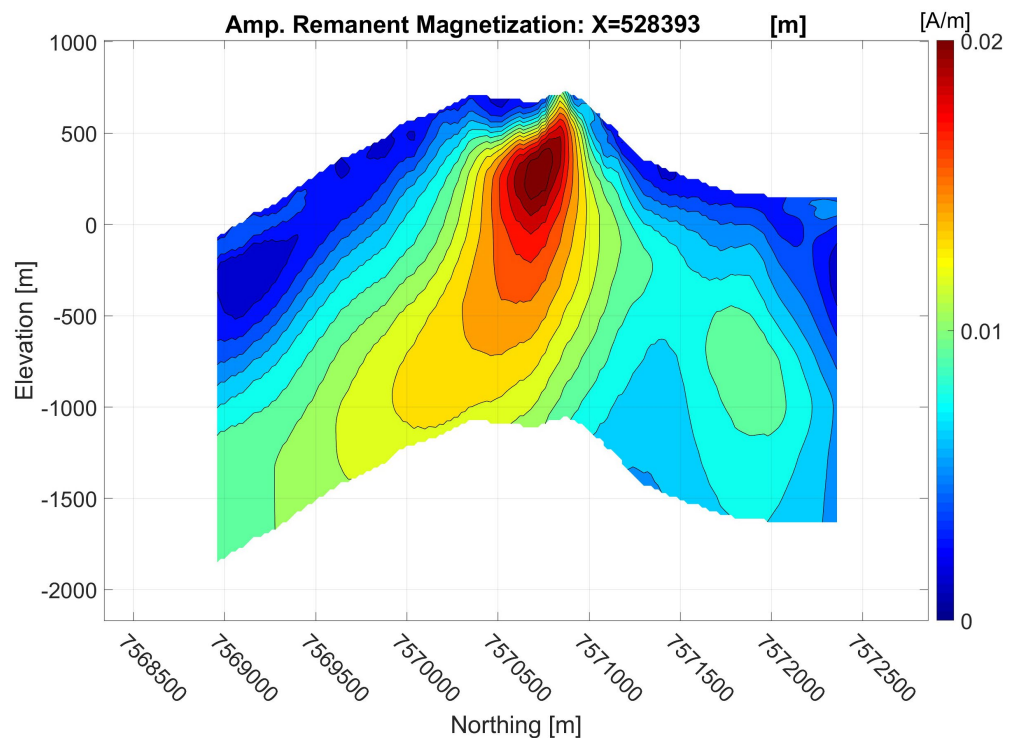


Figure 12. The vertical section was extracted from the 3D voxel model of the inverted amplitude of remanent magnetization. The location of the profile is shown in yellow in Figure 8.

Figure 13 shows the results for the MobileMT inversion—a vertical section of the inverted resistivity model through the porphyry system.

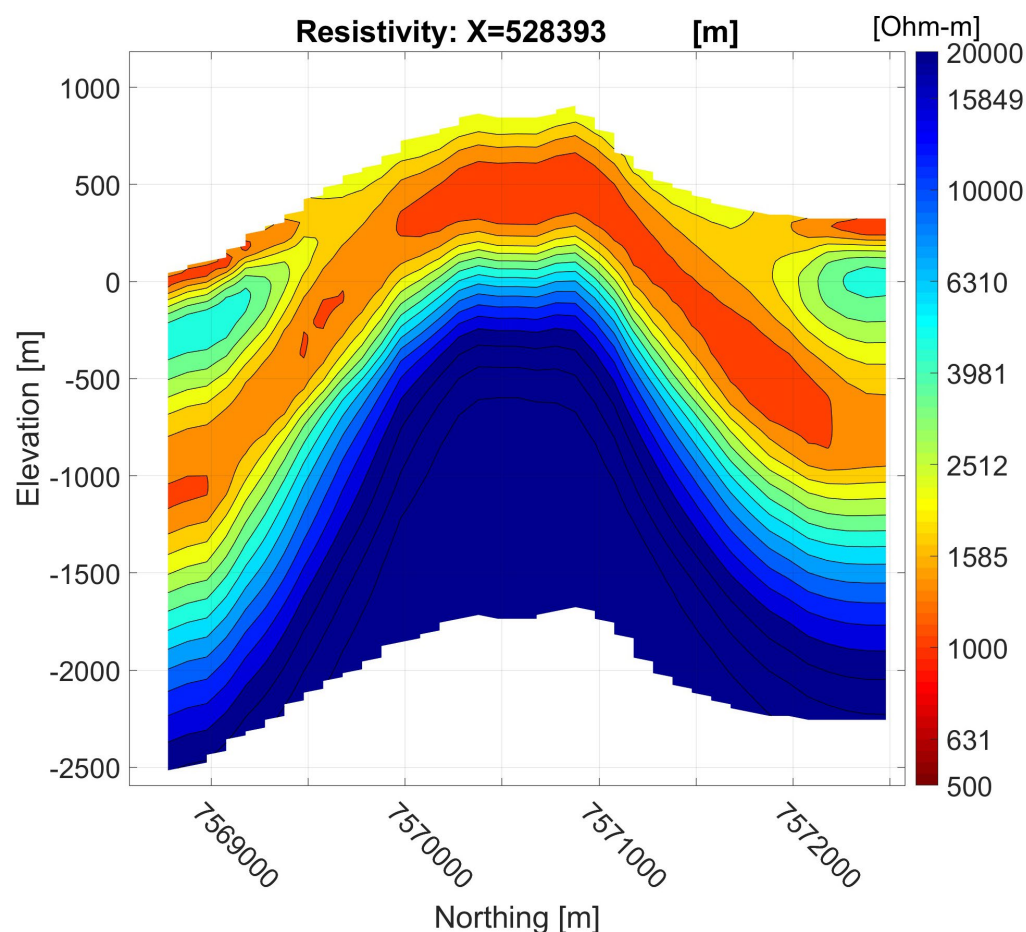


Figure 13. The vertical section was extracted from the 3D voxel model of the inverted resistivity. The location of the profile is shown in yellow in Figure 8. This vertical section showcases the porphyry system.

5. Discussion

When viewed as a system, the MobileMT and TMI inversion results provide complementary information that fits well with an expected porphyry model. According to [21], the plutonic core is expected to be magnetic and highly electrically resistive (1000 s–10,000 ohm-m). The potassic and phyllic alteration zones are typically moderately resistive (100 s–1000 s Ohm-m) because of the addition of sulfides and alteration to clays. The propylitic zone contains some alteration to clays and is also moderately resistive. The argillic zone is often the least resistive part because of the replacement of plagioclase and amphibole with kaolinite and montmorillonite [35], but quartz can also be pervasive, which increases the resistivity. The alteration zones are typically weak to non-magnetic.

Figure 14 shows the recovered electrical resistivity as a vertical section (same as Figure 12), with the remanent magnetization as the red isobody. The remanent isobody indicates values above 0.0125 A/m. The resistivity section shows two zones of reduced resistivity, one in the near surface indicating weathering and another zone at depth blanketing a very resistive area. This is interpreted to be alteration of the host rock to clays and the addition of sulfides, both of which will suppress the resistivity. Porphyry deposits often contain sulfide minerals such as chalcopyrite (copper), pyrite, or bornite, which can contribute to conductivity due to their metallic nature. Additionally, alteration minerals like sericite, clay minerals, or carbonates can also enhance conductivity. The remanent magnetization directly images the intrusive complex, which shows an elevated remanent response. The more conductive sheet imaged in the resistivity model closely caps the magnetic body.

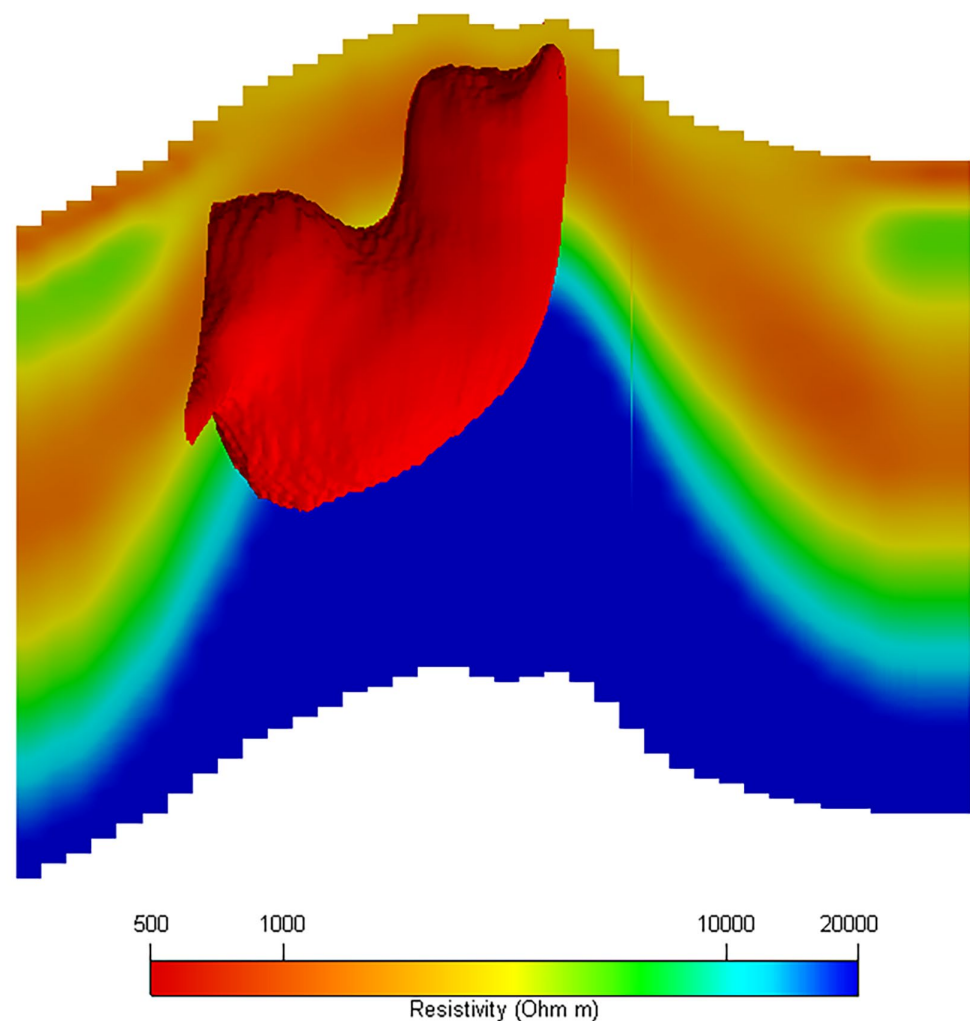


Figure 14. A west-facing view of resistivity (slice) and superposed remanent magnetization (red isobody). The red isobody indicates remanent values above 0.0125 A/m. This 3D figure is for illustrative purposes. The resistivity slice is in the same location as Figure 12.

The vertical sections in Figures 10 and 11 image the same vertical section as Figure 14, but they show susceptibility and induced magnetization, respectively. Both of these models show higher magnetism in areas of reduced resistivity. These may be imaging magnetic sulfides, such as pyrrhotite or magnetite, formed at a different time than the main intrusion.

Figure 15 presents a geological schematic based on the interpretation of the geophysical data. We can see the same lithologies apparent in the conductive sheet component of the porphyry system, as well as in the susceptibility and induced magnetization models. In contrast, the resistive core is apparent only in the remanent magnetization model.

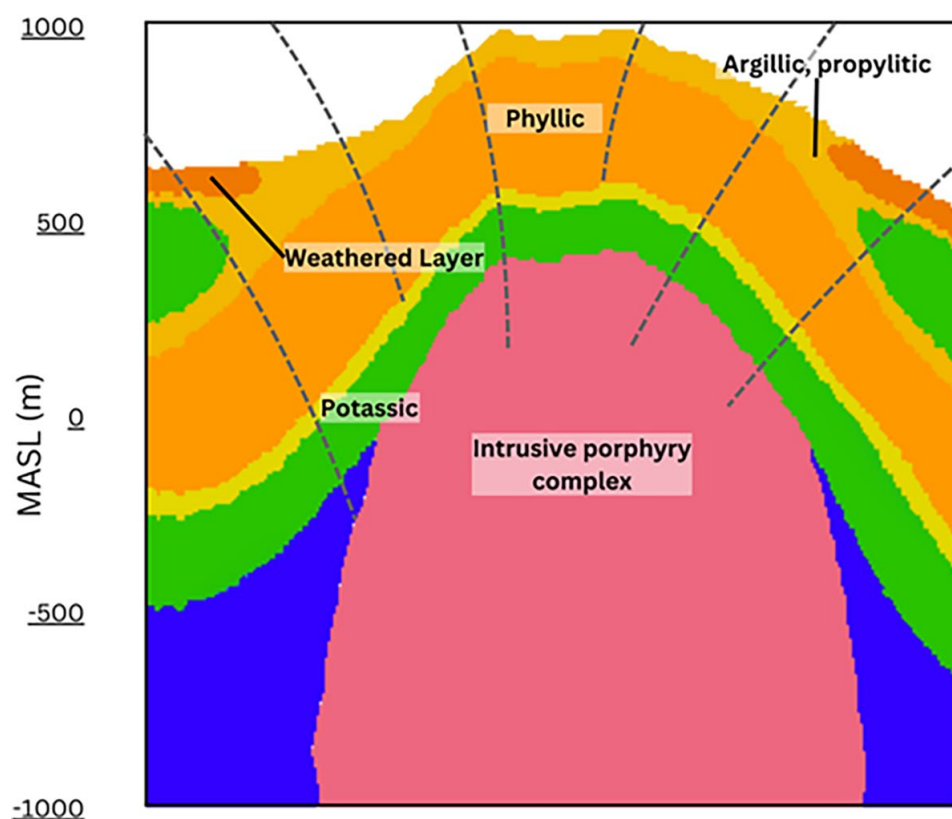


Figure 15. Schematic geological interpretation of the geophysical models. The combination of the resistivity and magnetic properties coalesce into a useful geological model.

6. Conclusions

The developed 3D geophysical models from full 3D inversion of multiphysics data paint a clear picture of a porphyry deposit. The inclusion of remanence in the TMI data interpretation was instrumental in developing accurate physical property models. A full 3D inversion of the MobileMT data was required to image the resistive core, as evidenced by the 3D nature of the targeted porphyry deposit. For 3D bodies, 3D inversion is necessary to properly fit the data and image the structures. Conventional TMI inversion is good for resolving magnetic anomalies without the presence of remanent magnetization; however, the remanent magnetization model proved to be the most useful for imaging the porphyry core directly. In fact, the remanent magnetization model produced anomalies that fit the conductive sheets in the resistivity model like a glove. The conductive sheet may have resulted from the presence of conductive minerals or alteration products. The resistive core represents less mineralized or unaltered rock.

The airborne geophysical platform used here included both TMI and MobileMT data acquisition systems. These two systems are flown concurrently, reducing costs and simplifying logistics, and providing two independent physical property measurements that are complementary for the exploration of porphyry systems. MobileMT is sensitive to deep structures (>500 m) and resistive bodies (1000 s–10,000 s ohm-m), which cannot be said of active airborne EM systems. These characteristics are important for the exploration of targets similar to porphyries and become even more important as the industry moves away from targeting individual deposits and toward full minerals systems exploration and development.

Author Contributions: Conceptualization, M.S.Z. and H.E.S.; methodology, M.S.Z., A.G., M.J. and L.C.; software, A.G. and M.J.; validation, M.S.Z., A.G., M.J., H.E.S. and L.C.; resources, A.P. and H.E.S.; data curation, A.G. and M.J.; writing—original draft, M.J. and L.C.; writing—review and editing, M.S.Z. and H.E.S.; visualization, M.J.; supervision, M.S.Z.; project administration, M.S.Z.; funding acquisition, M.S.Z. and H.E.S. All authors have read and agreed to the published version of the manuscript.

Funding: This research was funded by TechnoImaging, LLC, Vanguard Geophysics, Greenland Silver Moly Resources ApS, and 21st NORTH ApS.

Data Availability Statement: The datasets presented in this article are proprietary and not available.

Acknowledgments: The authors acknowledge TechnoImaging, LLC, Vanguard Geophysics, Greenland Silver Moly Resources ApS, 21st NORTH ApS, and Expert Geophysics Limited for their support of this research and their permission to publish it.

Conflicts of Interest: Authors Michael Jorgensen, Michael S. Zhdanov, Alex Gribenko, Leif Cox were employed by the TechnoImaging, LLC Company. Author Alexander Prikhodko was employed by the Expert Geophysics Limited Company. The remaining authors declare that the research was conducted in the absence of any commercial or financial relationships that could be construed as a potential conflict of interest.

References

1. Thaarup, S.M.; Poulsen, M.D.; Thorsøe, K.; Keiding, J.K. *Study on Arctic mining in Greenland*; Ministry of Economic Affairs and Employment of Finland: Helsinki, Finland, 2020.
2. Chen, T.; Hodges, G.; Miles, P. MULTIPULSE—high resolution and high power in one TDEM system. *Explor. Geophys.* **2015**, *46*, 49–57. [\[CrossRef\]](#)
3. Eadie, T.; Legault, J.M.; Plastow, G.; Prikhodko, A.; Tishin, P. VTEM ET: An improved helicopter time-domain EM system for near surface applications. *ASEG Ext. Abstr.* **2018**, *2018*, 1–5. [\[CrossRef\]](#)
4. Harvey, T. Minerals geophysics. *Preview* **2023**, *225*, 33–36. [\[CrossRef\]](#)
5. Ward, S.H. AFMAG—Airborne and ground. *Geophysics* **1959**, *24*, 761–787. [\[CrossRef\]](#)
6. Gribenko, A.V.; Zhdanov, M.S.; Cox, L.H.; Wilson, G.A.; Legault, J.; Zhao, S.; Fisk, K. 3D inversion of AirMt AFMAG data. In *SEG International Exposition and Annual Meeting*; SEG: Houston, TX, USA, 2012; SEG-2012-1261.
7. Holtham, E.; Oldenburg, D.W. Three-dimensional inversion of ZTEM data. *Geophys. J. Int.* **2010**, *182*, 168–182. [\[CrossRef\]](#)
8. Legault, J.M.; Jahandari, H.; Ebert, S. ZTEM natural field EM and magnetic survey results over the Berg porphyry copper project, Huckleberry district, British Columbia. In *Second International Meeting for Applied Geoscience & Energy*; Society of Exploration Geophysicists and American Association of Petroleum Geologists: Houston, TX, USA, 2022; pp. 1605–1609.
9. Lo, B.; Legault, J.; Kuzmin, P.; Fisk, K. Advances in airborne EM: Introducing ZTEM. In *11th SAGA Biennial Technical Meeting and Exhibition*; European Association of Geoscientists & Engineers: Utrecht, The Netherlands, 2009; cp-241-00023.
10. Prikhodko, A.; Bagrianski, A.; Kuzmin, P.; Sirohey, A. Natural field airborne electromagnetics—History of development and current exploration capabilities. *Minerals* **2022**, *12*, 583. [\[CrossRef\]](#)
11. Prikhodko, A.; Bagrianski, A.; Wilson, R.; Belyakov, S.; Esimkhanova, N. Detecting and recovering critical mineral resource systems using broadband total-field airborne natural source audio frequency magnetotellurics measurements. *Geophysics* **2024**, *89*, WB13–WB23. [\[CrossRef\]](#)
12. Sattel, D.; Witherly, K.; Kaminski, V. A brief analysis of MobileMT data. In *SEG International Exposition and Annual Meeting*; SEG: Houston, TX, USA, 2019; D043S102R007.
13. Witherly, K.; Kelley, K.D.; Golden, H.C. Geophysical expressions of ore systems—Our current understanding. In *Special Publications of the Society of Economic Geologists*; Society of Economic Geologists: Littleton, CO, USA, 2014; Volume 18, pp. 177–208.
14. Cox, L.H.; Zhdanov, M.S.; Prikhodko, A. Inversion for 3D Conductivity and Chargeability Models Using EM Data Acquired by the New Airborne TargetEM System in Ontario, Canada. *Minerals* **2024**, *14*, 237. [\[CrossRef\]](#)
15. Ellis, R.G. Inversion of airborne electromagnetic data. *Explor. Geophys.* **1998**, *29*, 121–127. [\[CrossRef\]](#)
16. Ellis, R.G.; de Wet, B.; Macleod, I.N. Inversion of magnetic data for remanent and induced sources. *ASEG Ext. Abstr.* **2012**, 1–4.
17. Jorgensen, M.; Zhdanov, M.S. Recovering Magnetization of Rock Formations by Jointly Inverting Airborne Gravity Gradiometry and Total Magnetic Intensity Data. *Minerals* **2021**, *11*, 366. [\[CrossRef\]](#)
18. Lelièvre, P.G.; Oldenburg, D.W. A 3D total magnetization inversion applicable when significant, complicated remanence is present. *Geophysics* **2009**, *74*, L21–L30. [\[CrossRef\]](#)
19. Li, Y.; Shearer, S.E.; Haney, M.M.; Dannemiller, N. Comprehensive approaches to 3D inversion of magnetic data affected by remanent magnetization. *Geophysics* **2010**, *75*, L1–L11. [\[CrossRef\]](#)
20. Zhu, Y.; Zhdanov, M.S.; Čuma, M. Inversion of TMI data for the magnetization vector using Gramian constraints. In *SEG Technical Program Expanded Abstracts*; Society of Exploration Geophysicists: Houston, TX, USA, 2015; pp. 1602–1606.

21. Witherly, K.E. What lies beneath? A reflection on the porphyry copper exploration model. *ASEG Ext. Abstr.* **2019**, *2019*, 1–4. [\[CrossRef\]](#)
22. Dawes, P.R. The bedrock geology under the Inland Ice: The next major challenge for Greenland mapping. *GEUS Bull.* **2009**, *17*, 57–60. [\[CrossRef\]](#)
23. Bridgwater, D.; Austrheim, H.; Hansen, B.T.; Mengel, F.; Pedersen, S.; Winter, J. The Proterozoic Nagssugtoqidian mobile belt of Southeast Greenland; a link between the eastern Canadian and Baltic shields. *Geosci. Can.* **1990**, *17*, 305–310.
24. Brooks, C.K. Rifting and doming in southern East Greenland. *Nature* **1973**, *244*, 23–25. [\[CrossRef\]](#)
25. Saunders, A.D.; Fitton, J.G.; Kerr, A.C.; Norry, M.J.; Kent, R.W. The North Atlantic Igneous Province. In *Large Igneous Provinces: Continental, Oceanic, and Planetary Flood Volcanism*; Mahoney, J.J., Coffin, M.F., Eds.; American Geophysical Union: Washington, DC, USA, 1997; Volume 100, pp. 45–93.
26. Deer, W.A.; Kempe, D.R.C. Geological investigations in East Greenland, Part XI, The minor peripheral intrusions, Kangerlussuaq, East Greenland. *Medd Grønland* **1976**, *197*, 1–25.
27. Riishuus, M.S.; Peate, D.W.; Tegner, C.; Wilson, J.R.; Brooks, C.K.; Harris, C. Temporal evolution of a longlived syenitic centre: The Kangerlussuaq Alkaline Complex, East Greenland. *Lithos* **2006**, *92*, 276–299. [\[CrossRef\]](#)
28. Mutschler, F.E.; Wright, E.G.; Ludington, S.; Abbott, J.T. Granite molybdenite systems. *Econ. Geol.* **1981**, *76*, 874–897. [\[CrossRef\]](#)
29. Jorgensen, M.; Zhdanov, M.S.; Parsons, B. 3D focusing inversion of full tensor magnetic gradiometry data with Gramian regularization. *Minerals* **2023**, *13*, 851. [\[CrossRef\]](#)
30. Zhdanov, M.S. *Inverse Theory and Applications in Geophysics*; Elsevier Science: Amsterdam, The Netherlands, 2015.
31. Berdichevsky, M.N.; Zhdanov, M.S.; Feinberg, E.B. Electrical conductivity functions in the magnetotelluric and magnetovariation methods. *Ann. Geophys.* **1976**, *32*, 301–318.
32. Zhdanov, M.S. *Foundations of Geophysical Electromagnetic Theory and Methods*, 2nd ed.; Elsevier Science: Amsterdam, The Netherlands, 2018.
33. Gribenko, A.; Green, A.M.; Cuma, M.; Zhdanov, M.S. Efficient 3D inversion of MT data using integral equations method and the receiver footprint approach: Application to the large-scale inversion of the Earthscope MT data. In *SEG International Exposition and Annual Meeting*; SEG: Houston, TX, USA, 2010; SEG-2010-0644.
34. Pare, P.; Gribenko, A.V.; Cox, L.H.; Čuma, M.; Wilson, G.A.; Zhdanov, M.S.; Legault, J.; Smit, J.; Polome, L. 3D inversion of SPECTREM and ZTEM airborne electromagnetic data from the Pebble Cu–Au–Mo porphyry deposit, Alaska. *Explor. Geophys.* **2012**, *43*, 104–115. [\[CrossRef\]](#)
35. Guilbert, J.M.; Park, C.F., Jr. *The Geology of Ore Deposits*; Waveland Press: Long Grove, IL, USA, 2007.

Disclaimer/Publisher’s Note: The statements, opinions and data contained in all publications are solely those of the individual author(s) and contributor(s) and not of MDPI and/or the editor(s). MDPI and/or the editor(s) disclaim responsibility for any injury to people or property resulting from any ideas, methods, instructions or products referred to in the content.